

Quasiperiodic Sn layer

Sudipta Roy Barman¹, M. Maniraj^{1†}, Abhishek Rai^{1†}, Marian
Krajčí², Pampa Sadhukhan¹, Vipin Kumar Singh¹, Katariina Puski³,
Deborah L. Schlager⁴, Thomas A. Lograsso⁴, Ajay Kumar Shukla⁵

¹*UGC-DAE Consortium for Scientific Research,
Khandwa Road, Indore - 452001, Madhya Pradesh, India*

²*Institute of Physics, Slovak Academy of Sciences,
Dúbravská cesta 9, SK-84511 Bratislava, Slovak Republic*

³*LUT School of Engineering Science,
P.O. Box 20, FIN-53851 Lappeenranta, Finland*

⁴*Division of Materials Sciences and Engineering,
Ames Laboratory, Ames Iowa 50001-3020, USA*

⁵*CSIR-National Physical Laboratory,
Dr. K. S. Krishnan Road, New Delhi - 110012, India and*

[†]*Both the authors have contributed equally to this work.*

Abstract

Quasicrystalline materials exhibit aperiodic long range order and forbidden rotational symmetries, but show sharp diffraction spots. Although quasicrystals were discovered more than 30 years ago, elemental quasicrystals have remained elusive so far. Here, we demonstrate unique characteristics of an elemental Sn layer: it adopts a buckled five-fold quasiperiodic (*QP*) structure that is different from the icosahedral (*i*)-Al-Pd-Mn substrate. The pseudogap in the electronic states around the Fermi level that stabilizes a quasicrystal, is further deepened in the Sn layer compared to the substrate. On the basis of density functional theory, we relate this intriguing observation to the buckling with enhanced covalency and sp^3 bonding between Sn atoms. Quasiperiodicity is observed up to 1.4 nm (5 ML) at 100 K, a thickness regime where the influence of the substrate potential is negligible.

PACS numbers: 71.23.Ft, 79.60.Dp, 61.05.jh, 68.37.Ef

The mathematical concept of aperiodic ordering and the discovery of quasicrystals brought paradigm shift in crystallography[1, 2]. Quasiperiodicity has been observed in different inter metallic compounds[3], binary nano-particle super lattices[4], oxide thin film[5] and large molecular assemblies[6, 7]. Technological importance of quasicrystals arise from their low frictional coefficient, heat insulation and photonic band gap[8, 9]. Quasicrystals exhibit interesting electronic properties such as low conductivity and specific heat[10]. A recent exciting finding is its nontrivial topological property originating from higher dimensions[11]. However, the chemical complexity of quasiperiodic (QP) materials discovered so far hinders the basic understanding of their unusual properties. An elemental quasicrystal would be best suited for this purpose. Efforts in this direction for over a decade have involved the use of quasicrystalline substrates as a template to grow QP elemental layers[12–22]. Pseudomorphic growth 1 monolayer (ML) quasiperiodic Sn has been reported in the past on i -Al-Cu-Fe[20] and decagonal (d)-Al-Ni-Co[19]. In fact, in most of the studies reported so far, the first wetting layer has been reported to be quasiperiodic with a structure similar to the substrate.

A single layer of Sn with a honeycomb structure has been shown to be a quantum spin Hall insulator with a sizable nontrivial gap opened by spin-orbit coupling[23]. In analogy to graphene, this has been named stanene. However, while graphene is planar, stanene is buckled and stabilized by sp^3 bonding. Recently, stanene has been successfully grown on $\text{Bi}_2\text{Te}_3(111)$ substrate[24]. A density functional theory (DFT) study predicted pseudomorphic and QP growth of Sn on i -Al-Pd-Mn[21]. But to our surprise, we find that the QP structure of the Sn layer deposited on i -Al-Pd-Mn is buckled with enhanced sp^3 hybridization which we refer to as QP stanene-like configurations. The other unique characteristics of Sn/ i -Al-Pd-Mn is a deeper pseudogap in the photoemission spectral function near Fermi level compared to i -Al-Pd-Mn (known to be one of the most stable quasicrystal) and up to 1.4 nm thickness of the QP Sn layer where the influence of the substrate is negligible indicate the possibility that elemental Sn might exist as a quasicrystal in the bulk form.

In Fig. 1, we establish the unusual QP ordering of Sn on i -Al-Pd-Mn through LEED. The pattern of bare i -Al-Pd-Mn in Fig. 1A exhibits two sets of ten spots, inner and outer[28]. A blue pentagon connects the intense (10000) spots of the inner set. For 0.3 – 0.5 ML Sn coverage, although the LEED pattern is similar to the bare surface, a careful inspection reveals that the (000 $\bar{1}$ 0) spots are diminished in intensity (Figs. 1B, C). The most

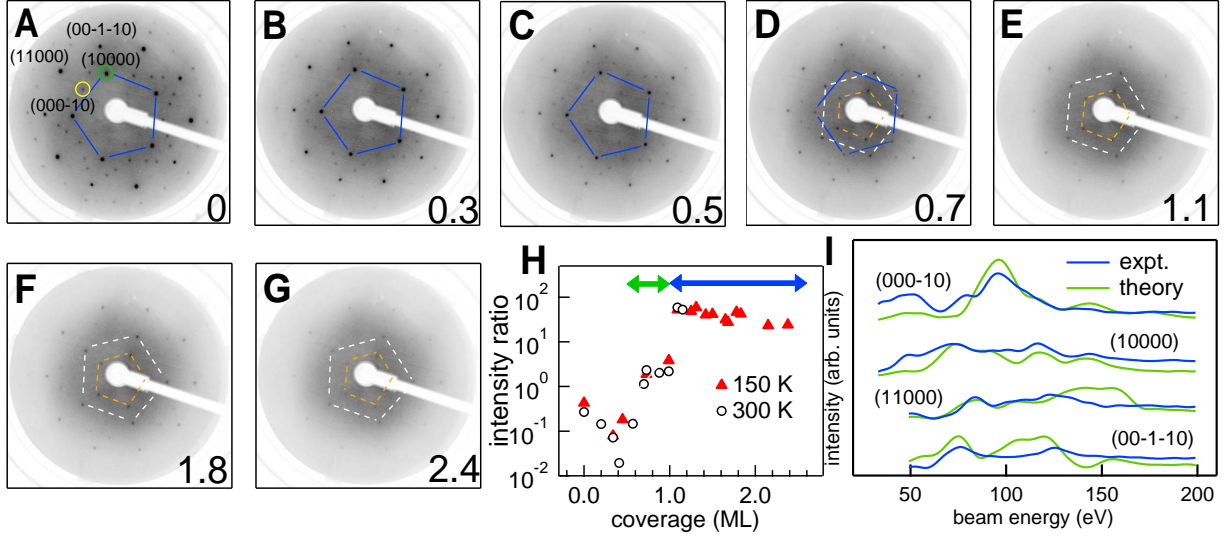


FIG. 1: **Low energy electron diffraction:** **A-G**, *LEED* patterns of *Sn/i-Al-Pd-Mn* at beam energy of 81 eV as a function of coverage indicated in ML at the bottom right corner at 150 K. Miller indices of some of the spots are shown in (A), the (10000) and (000 $\bar{1}$ 0) spots are highlighted by green and yellow circles, respectively. **H**, Intensity ratio of (000 $\bar{1}$ 0) and (10000) spots that represent the reconstructed Sn layer and the bare surface, respectively. **I**, Experimental intensity versus beam energy (IV) curves for 1 ML *Sn/i-Al-Pd-Mn* compared with the theoretical calculation.

interesting change is observed between 0.7 to 1.1 ML (Fig. 1D,E): the (000 $\bar{1}$ 0) intensities increase dramatically (white dashed pentagon), while the (10000) intensities decrease (blue pentagon). Furthermore, a set of five spots appears, which was hardly visible earlier, forming a smaller pentagon (orange dashed) with an orientation rotated 36° with respect to the blue pentagon. Henceforth, we call it the innermost set. As the Sn coverage is increased beyond a monolayer (Fig. 1F,G), the spots joined by white and orange dashed pentagons remain clearly visible, while the (10000) spots become inconspicuous. Note that the Sn layer LEED patterns clearly exhibit five fold symmetry and the distance of the innermost, inner and outer set of spots from (0, 0) is in the ratio of $1:\tau:\tau^2$, where τ is the golden mean ($= 1.618$), further confirming *QP* nature of the Sn layer. At other beam energies too, the LEED pattern is clearly modified (Supplementary Fig. S1). The intensity versus beam energy (IV) curves are completely different between 1 ML Sn and *i-Al-Pd-Mn* (Supplementary Fig. S2), demonstrating the structural differences between the two.

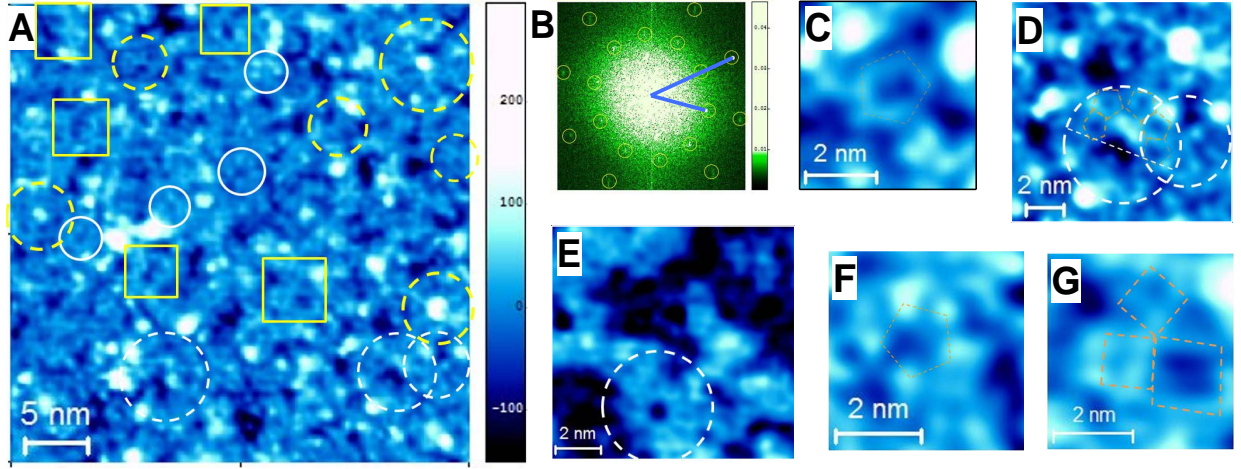


FIG. 2: **Scanning tunneling microscopy:** **A**, High resolution STM topography image with tunneling current (I_T) = 0.2 nA and bias voltage (U_T) = 1.5 V for 1 ML Sn/*i*-Al-Pd-Mn after low-pass Fourier transform (FT) filtering; various motifs are marked by circles and rectangles (the raw image is Fig. S5 a(ii) of Supplementary). The color scale with the height in picometers is shown on the right. **B**, FT of the STM image shown in **A**. **C**, Pentagonal (P) tile, and **D**, the crown motif from **A**. **E**, STM image of 0.6 ML Sn/*i*-Al-Pd-Mn after low-pass FT filtering (the raw image is Fig. S5 c(ii) of Supplementary). **F**, The vertex bulged pentagonal tile and **G**, the rhombus motif (dashed yellow lines) from **A**.

In analogy with the reconstruction of an adlayer on a crystalline substrate, this characteristic of the Sn layer is termed as a *QP* reconstruction. The reconstruction is completed at ≥ 1 ML and the LEED pattern remains essentially unchanged for higher coverages, although the sharpness and intensity of the spots decrease. The reconstruction as a function of coverage can be quantitatively expressed by the intensity ratio of the (000 $\bar{1}$ 0) and (10000) spots, representing the reconstructed Sn layer and the *i*-Al-Pd-Mn surface, respectively (Fig. 1H). The region depicted by a green double arrow from 0.4 to 1 ML represents the intermixed region where the LEED signal from both the substrate as well as the Sn layer are observed, and beyond 1 ML (blue double arrow) the LEED is fully reconstructed. The reconstruction is independent of the substrate temperature 100 K to 300 K, see Fig. S3 of Supplementary for LEED at 300 K.

A comparison of a high resolution STM image of 1 ML Sn/*i*-Al-Pd-Mn (Fig. 2A) with that

of *i*-Al-Pd-Mn (Supplementary Fig. S4) shows striking differences between the two. The Sn layer exhibits larger corrugation that is quantified by the root mean square roughness (S_q): for the Sn layer S_q is 0.04 nm, whereas for *i*-Al-Pd-Mn it is 0.023 nm. Moreover, comparing two images recorded under similar tunneling conditions (Supplementary Fig. S4), the full width at half maximum of the height distribution histogram is 0.08 nm for the Sn layer, while it is significantly smaller (0.05 nm) for *i*-Al-Pd-Mn. The Fourier transform of the STM image in Fig. 2A shows clear evidence of QP ordering with two sets of spots of tenfold symmetry highlighted by yellow circles, whose distance from the center (shown by blue lines) is in the ratio of τ (Fig. 2B). The most prevalent tile in the Sn layer is a pentagon (P) with a central dark region (Fig. 2C). The length of the sides of the P -tiles exhibits a rather broad Gaussian distribution centered around 0.7 nm. The P -tiles often seem irregular, which is another indication that these are buckled *i.e.* out of the two dimensional plane. These tiles assemble into different motifs highlighted by white and yellow dashed circles in Fig. 2A. The most spectacular among them is an incomplete tenfold circular congregation of P -tiles around a central region marked by white dashed circles: five P -tiles appear around a bright center forming a half-circle that we refer to as a crown motif (Fig. 2D). Height profiles along the sides of the P -tiles show that these are buckled with a corrugation of 0.06 nm. The P -tiles are also observed at lower coverages; indeed, for 0.6 ML Sn in Fig. 2E, the P -tiles abound and even a crown motif is observed, as highlighted by a white dashed circle. Vertex bulged pentagonal tiles with a side length of about 1.1 nm (Fig. 2F, white circles in Fig. 2A) and rhombic tiles (Fig. 2G) are also observed. The rhombic tiles are highlighted by yellow rectangles in Fig. 2A.

Fig. 3A, B show that the second layer of Sn grows by gradually spreading out from their points of nucleation. The motifs are similar to the 1st layer (Fig. 2): P -tiles (yellow arrows) congregate into crown motifs (white dashed circle) and vertex bulged pentagonal motifs (white circle) (Fig. 3C) are observed. The height distribution histogram and the height profiles in Fig. 3D, E clearly show that the second layer is ≈ 0.2 nm thick and importantly, no islands of larger height are observed. Fig. 3F shows an almost completely formed second layer of Sn. The motifs are similar to those in Fig. 2 and these are highlighted in a zoomed image (Fig. 3G). A height profile (Fig. 3H) along *e-f* gives the total height of the two layers to be 0.43 nm, while 0.8 nm is the step height of the substrate. The quasiperiodicity of the second layer is confirmed by the FT (Fig. 3I) that shows two sets of spots (yellow circles)

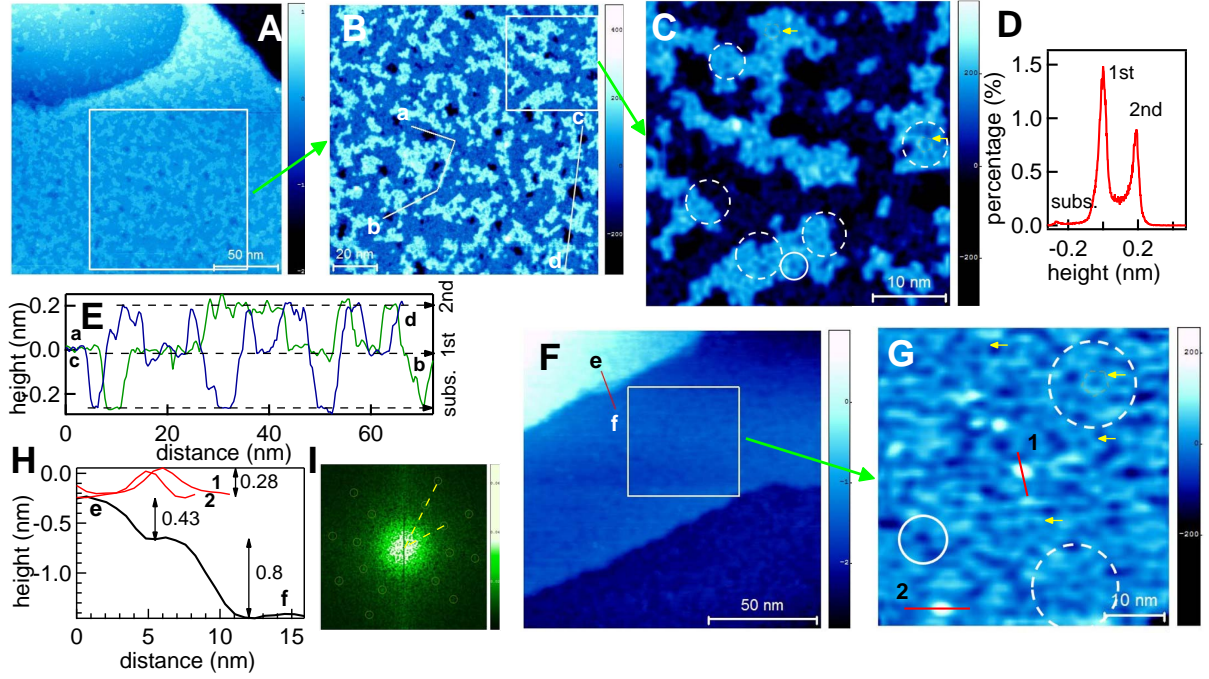


FIG. 3: **Scanning tunneling microscopy of the second Sn layer:** **A, B**, *High resolution STM topography image of 1.4 ML Sn/i-Al-Pd-Mn with $I_T = 0.6$ nA and bias voltage (U_T) = -2.6 V and C*, a zoomed part of **B**, after low-pass Fourier transform (FT) filtering, yellow arrows show the *P* tiles, while the different motifs are marked by dashed and solid circles. **D**, height distribution histogram of **B** and **E**, height profiles along *a-b* and *c-d*. **F**, STM topography image of 2 ML Sn; **G**, a zoomed region after low-pass FT filtering showing different motifs (yellow arrows and circles). **H**, Height profile along *e-f* (black line) showing the height of the double Sn layer in nm; and those along **1** and **2** (red lines) show the height of the nucleation regions of the third layer. **I**, FT of a STM image for nearly 2 ML Sn/i-Al-Pd-Mn. A comparison of the FT filtered and raw images is provided in Supplementary Figure S9.

with tenfold symmetry, whose distance from the centre (shown by white dashed lines) is in ratio of τ . Thus, STM unambiguously demonstrates *QP* growth up to the second layer at room temperature. Interestingly, the bright regions in Fig. 3G demonstrate nucleation of the third layer and the height profiles along lines (**1** and **2** in Fig. 3H) show its thickness to be 0.28 nm, which is very close to the Sn-Sn bond length (0.281 nm). The second layer also exhibits buckling, and this is evident from the S_q value of 0.05 nm that is somewhat larger than the first layer (0.04 nm).

It is important to note that none of the motifs observed in Sn layer in Figs. 2, 3 are observed on *i*-Al-Pd-Mn and vice-versa. These are also different from the motifs in Sn/*i*-Al-Cu-Fe[20] or an other *QP* layer reported until date. Thus, STM demonstrates that the structure of the Sn layer is unique and is different from *i*-Al-Pd-Mn. Since the Sn layer is buckled, the known *QP* tilings for a two-dimensional plane are somewhat inadequate in this case. DFT calculations presented below establish that the buckling has its origin in the electronic structure of Sn.

While from STM it is evident that the Sn layer exhibits buckling, an important question is whether this could also explain the reconstruction shown by LEED (Fig. 1). To address this issue, we have performed a theoretical IV analysis using a nearly planar pentagonal Sn cluster consisting of two pentagons based on DFT[22] as the starting structure (Fig. 5G). In Fig. 1I, the theoretical and experimental IV curves for 1 ML Sn exhibit reasonable agreement with Pendry reliability factor (R_P) \approx 0.3 for (10000), (000 $\bar{1}$ 0) and (11000), while for (00 $\bar{1}$ 10) it is 0.62. The converged structure is considerably buckled where the height difference between the highest and the lowest Sn atoms is 0.15 nm. In fact, if the buckling of the Sn layer is not allowed, the calculated IV curves completely fail to resemble the experimental data (Supplementary Fig. S6). Although the Sn adlayer grows in the same reciprocal lattice as the substrate, it is the buckling that makes the structure different compared to the substrate. However, the positions of the LEED spots come from the lateral arrangement of Sn atoms, which are steered by the underlying substrate, so this is why we do not see any extra spots, only changes in intensity are observed. Our LEED IV analysis thus establishes that the Sn layer is buckled.

While growth of a quasiperiodic second layer of Sn is established from STM and LEED discussed above, at about 100 K, a thicker Sn layer could be grown. We studied this low temperature growth by XPS and LEED. The intensities of the Sn 3*d* and Al 2*p* XPS core-level spectra as function of deposition have been fitted with exponential functions and the quality of the fit is excellent (Fig. 5A). It is well known that such exponential variation of adlayer as well as substrate core-level intensities portrays layer by layer growth. The maximum thickness of the Sn layer turns out to be about 2 nm, *i.e.* about 7 ML considering an upper limit of the thickness of a Sn layer to be 0.281 nm. It may be noted that layer by layer growth was not observed for Sn/*i*-Al-Cu-Fe[20], rather island growth was observed above 1 ML. This is because Sn deposition was done at a higher temperature of 573-623 K,

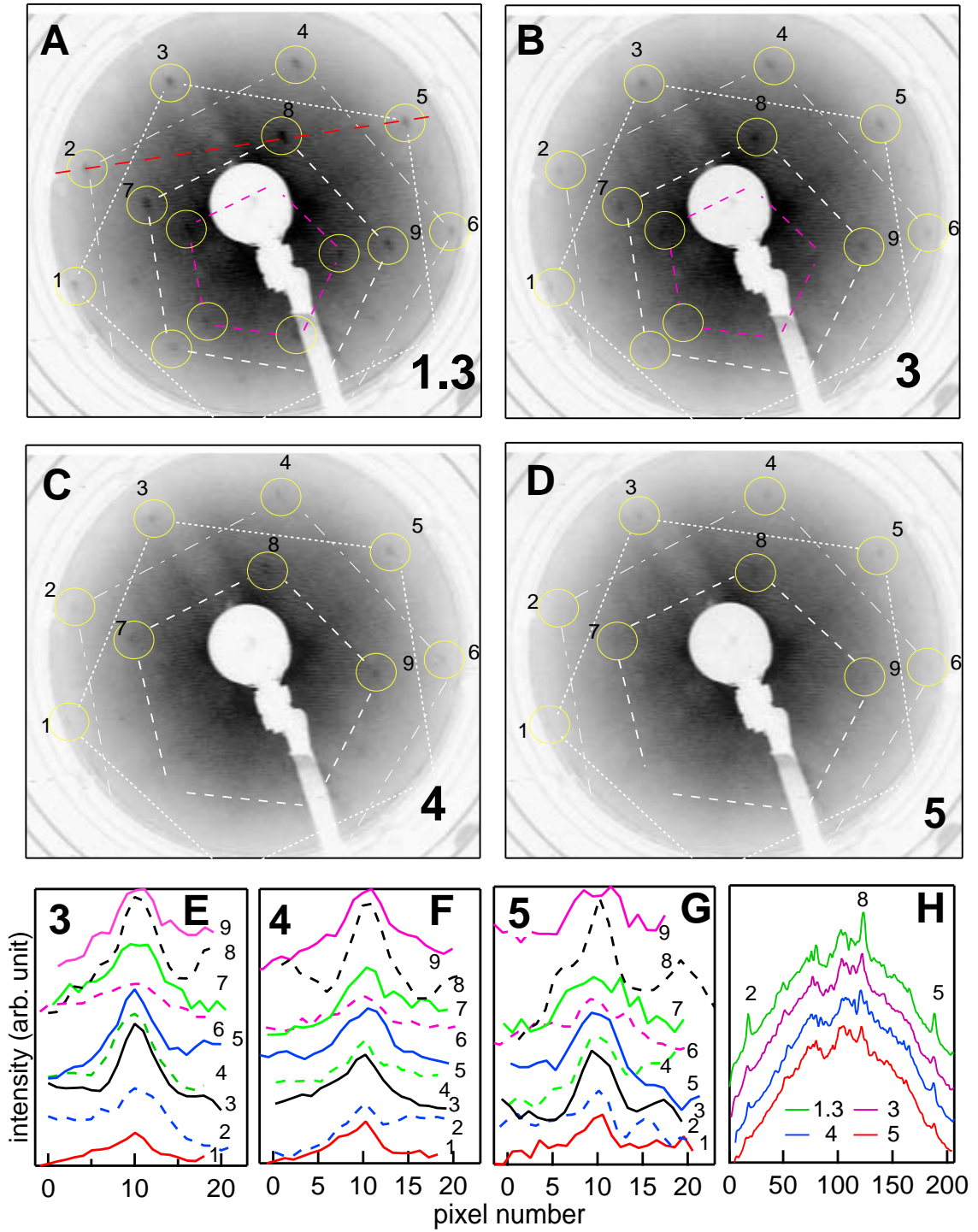


FIG. 4: Low energy electron diffraction for Sn layer grown at 100 K: A- D, *LEED patterns* of Sn/i-Al-Pd-Mn at beam energy of 80 eV in inverted scale at different coverages indicated at the bottom right corner. E- G, *Intensity profiles* (along lines shown in Supplementary Figure 8) depicting the intensities of the LEED spots for 3, 4, and 5 ML, respectively. H, *Intensity profiles* along the red dashed line shown Fig.4A) through the LEED spots numbered 2, 5 and 8.

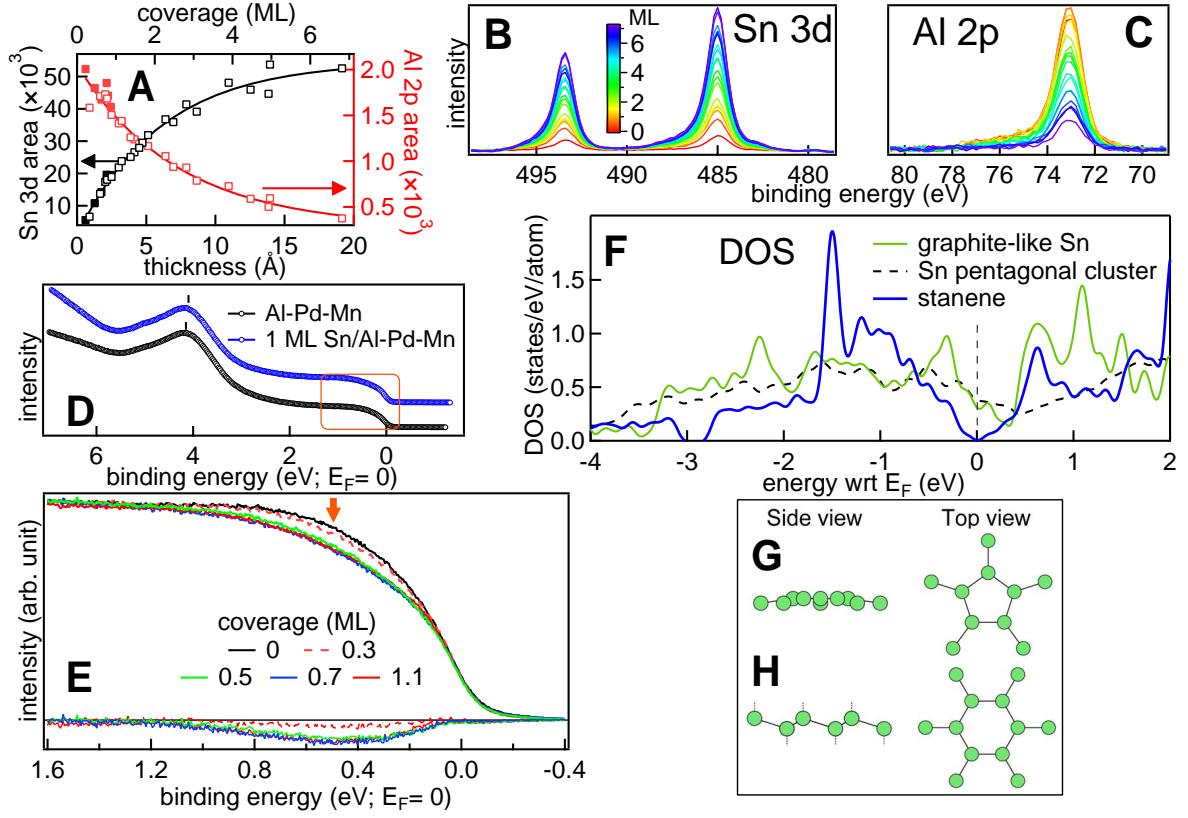


FIG. 5: **Photoemission spectroscopy and density functional theory:** **A**, The areas under **B**, Sn 3d and **C**, Al 2p core-level peaks as a function of Sn layer thickness at 100 K (open squares) and 300 K (filled squares). The continuous lines are fitted curves showing an exponential variation. **D**, The valence band spectra of Sn/*i*-Al-Pd-Mn using ultraviolet photoemission spectroscopy. **E**, The spectral shape close to the Fermi level (E_F) is shown along with the difference spectra taken between each Sn coverage and bare *i*-Al-Pd-Mn to demonstrate the deepening of the pseudogap. **F**, The DOS of graphite-like Sn, Sn pentagonal cluster and stanene. The side **G**, and top **H**, views of the nearly planar Sn pentagonal cluster and stanene.

where activated diffusion of Sn across terraces possibly resulted in clustering and island growth. Furthermore, our results are different from Sn/*i*-Al-Cu-Fe because *i*-Al-Cu-Fe and *i*-Al-Pd-Mn have large difference in their electronic structure and transport properties[27].

The LEED patterns of Sn deposited at 100 K are shown in Fig. 4. The LEED spots observed at 1.4 ML (Fig. 4A) are marked by yellow circles and are numbered 1–9. This pattern is similar to Fig. 1E. However, since this set of experiment was performed using a

different instrument, the patterns are off-centered and some spots in the lower part of the screen fall outside and are not observed. Nevertheless, QP order is clearly established, as shown by the white dashed pentagons joining the LEED spots. At 3 ML coverage, all the spots (1-9) are clearly observed, and the line profiles through each spot are shown in Fig. 4E. At 4 ML, the spots corresponding to the outer and inner pentagons that are visible at 1.4 ML, are also observed (Fig. 4F), although their intensities are somewhat diminished. However, the spots corresponding to the innermost pentagon are too weak to be observed. At 5 ML, all the spots (1- 9) are observed, as established by their line profiles (Fig. 4G), although considerably diminished in intensity. The gradual decrease in intensity of the LEED spots is related to enhanced roughness of the layer with increasing thickness.

Beyond 5 ML, some of the QP LEED spots are still observed, but enhanced background intensity makes them indeed hard to decipher. Furthermore, at different beam energies (50 to 80 eV), splitting or appearance of new spots are not observed (Supplementary Fig. S7 for 5 ML): at 50 eV, a set of spots (1-6) is observed, this is similar to the pattern at 53 eV for 1.1 ML (Supplementary Fig. S1 b(iii)). At 60 eV these spots move closer to the center. At 75 eV, new spots appear whose positions and intensities are similar to those at 80 eV. These LEED patterns (and in Fig. S1 of Supplementary) at different beam energies confirm that Sn layer has QP order and not rotational epitaxy where five cubic domains have orientational relationship with the quasicrystalline substrate. Another confirmation that QP order persists up to 5 ML is that the position of the spots remain unchanged with coverage. This is shown in Fig. 4H by the intensity profiles through the spots numbered 2, 8 and 5 for different coverages up to 5 ML. A sequential video stacking of LEED patterns is provided (5ML_Sn_Final.avi in Supplementary material) for the 1.4 nm (5 ML) layer. Here, the spots are clearly identified as these move towards the centre with increasing beam energy. Thus, present data indicate that quasiperiodicity exists up to 5 ML Sn/*i*-Al-Pd-Mn. Unlike in the present case, for Cu/*i*-Al-Pd-Mn[14], aperiodicity was observed only in one direction. Sn/*i*-Al-Pd-Mn is thus the thickest (1.4 nm) five-fold QP adlayer reported to date. Note that the effective potential of a solid including the exchange interaction term perpendicular to the surface is almost zero beyond unity Fermi wavelength[29]. Al and Mn that form the top layer of *i*-Al-Pd-Mn[28] have Fermi wavelengths of 0.36 nm and 0.37 nm, respectively. Surprisingly, Sn retains quasicrystallinity up to a thickness larger than the region of influence of the substrate potential.

Notably, the binding energies of both Sn 3*d* and Al 2*p* core-level photoelectron spectra remain unaltered up to the highest coverage *i.e.* 7 ML (Figs. 5B, C). Core-level binding energies are sensitive to the transfer of electronic charge from the adsorbate to the substrate, which obviously can be ruled out in this case. At low coverages, if the adsorbate-substrate interaction is larger than adsorbate-adsorbate interaction, generally the adlayer is homogeneously dispersed and a change in the binding energy of the adsorbate atom is observed. However, with increasing coverage, the adsorbate-adsorbate interaction dominates and this leads to a condensed island growth that is indicated by absence of any shift in the binding energy of the adsorbate. For example, below 1 ML, both Na and K were reported to form a dispersed phase on *i*-Al-Pd-Mn[16]. Absence of core level shift or change in shape excludes the possibility of any alloying or intermixing of Sn with the substrate. It also implies a propensity for condensed island growth[16], thus indicating the presence of strong adsorbate-adsorbate interaction. Evidence of condensed island growth is also shown by STM, where clustering of Sn atoms occur even at low coverages[39]. Fig. 5D depicts the valence band of Sn/*i*-Al-Pd-Mn, where the prominent peak at 4 eV binding energy arises from Pd 4*d*-like states. Its binding energy also remains unchanged between 0 and 1 ML Sn coverage lending further support to the above deduction.

The stability of quasicrystals has been related to the existence of a pseudogap in the electronic density of states (DOS) around the Fermi level (E_F) originating from the interaction between the Fermi surface and the quasi-Brillouin zone of the quasicrystal[25–27]. In the valence band spectrum of *i*-Al-Pd-Mn (Fig. 5D), the pseudogap was ascribed to the rounded shape of the spectral function close to E_F [26]. With Sn deposition, we observe an interesting change in its shape (red arrow in Fig. 5E): the intensity of the spectral weight decreases compared to bare *i*-Al-Pd-Mn, indicating a deepening of the pseudogap. This is also evident from the difference spectra in lower part of Fig. 5E. Interestingly, as the coverage approaches 1 ML, the spectral shape becomes almost invariant.

To understand why the pseudogap deepens and how it is related to the *QP* reconstruction, we have calculated the DOS and analyzed the nature of bonding in the Sn layer using DFT. In Fig. 5F, the DOS projected on to Sn atoms for the pentagonal Sn cluster (Fig. 5G) exhibits a broad pseudogap around E_F , with the minimum about 0.5 eV above E_F . In Fig. 5F, we further compare the DOS of the pentagonal Sn cluster with the DOS of Sn in the graphite structure with sp^2 bonding characteristics. The pseudogap of Sn in

the graphite-like structure is quite similar to that of the Sn pentagonal cluster and in both cases the minimum of the DOS is shifted above E_F . Thus, neither the nearly planar Sn pentagonal cluster nor the planar graphite-like Sn structure with sp^2 bonding can explain the deepening of the pseudogap observed in photoemission. In order to unravel this mystery, we compare the DOS of stanene (Fig. 5H) with that of the Sn pentagonal cluster in Fig. 5F. In contrast to the planar structure of graphene characterized by sp^2 bonds, in the honeycomb structure of stanene, the sp^3 bonds prefer threefold coordination of Sn atoms in a corrugated plane. The fourth sp^3 bond directed perpendicular to the corrugated plane can be saturated by some chemical functional groups[23] or by bonding with a substrate. The buckling of stanene is about 0.086 nm and depends partially also on the chemical environment[23].

Fig. 5F shows that the pseudogap of stanene is definitely more pronounced than the Sn pentagonal cluster. In fact, the DOS in stanene becomes almost zero at E_F . The common property of the QP Sn layer and stanene is that both are buckled structures, where the bonds with enhanced covalency prefer tetrahedral orientation and three of the neighboring Sn atoms are in the buckled plane. While in periodic stanene the inter atomic bonds form six-fold rings, in the reconstructed QP layer, bonds form five-fold rings and also other rings with different number of vertices. However, we accept that our arguments would be more convincing if we also present the stanene-like model structure and compare the calculated with experimental ones. On the other hand, construction of a realistic model of a quasicrystalline structure is a very difficult task. We note that although many quasicrystal phases have been observed, structure is available only for a very few of them. It is worth to note that in the structure with the stanene-like tetrahedral ordering the ratio between the first and second neighbor distances is $\sqrt{8/3}=1.633$, which almost coincides with the golden mean τ characterizing the quasiperiodic icosahedral ordering. The inter atomic bonding in the reconstructed Sn layer is different from the Pb layer [12, 17, 22]. Pb does not have $s - p$ hybridization since the s and p bands are clearly separated, and thus the bonding is mediated by p orbitals only. Here, the deepening of the pseudogap around E_F and the increased buckling of the adlayer at higher coverages could be thus interpreted as a signal of formation of stanene-like structures *i.e.* buckled structure with high covalency and sp^3 bonding between the Sn atoms. The larger buckling of the Sn layer, supported by the sp^3 bonds, could help to stabilize the QP ordering.

In conclusion, our work demonstrates unusual behavior of elemental Sn, a quasicrystalline

reconstruction exhibiting a QP arrangement of Sn atoms that is buckled and has predominant sp^3 bonding with high covalency. Photoemission spectroscopy shows that the pseudogap of the Sn layer is even deeper than i -Al-Pd-Mn, which is known to be the most stable quasicrystal. The enhanced stability of the Sn adlayer is explained by our DFT calculations to be related to its QP stanene-like configuration. This is an important result because to date no other pseudomorphic quasicrystalline adlayer has caused a deepening of the substrate pseudogap. This clearly suggests a greater stability of the Sn adlayer compared to other known pseudomorphic elemental quasicrystalline adlayers. Thus, it is obvious why Sn is the thickest (1.4 nm) quasiperiodic adlayer reported so far. The thickness extends beyond the potential of the substrate, indicating that Sn has a tendency to retain its quasicrystallinity. On the basis of these interrelated unique attributes of Sn, we believe that Sn is possibly the most suitable candidate in the search for elemental quasicrystallinity in the bulk form.

Methods

The single grain fivefold i -Al-Pd-Mn quasicrystal surface was prepared by repeated cycles of Ar^+ ions sputtering and annealing to about 930 K for 2–2.5 h. The cycles were repeated until sharp fivefold LEED pattern was observed. Sn (99.99% purity) was evaporated from a water cooled Knudsen evaporation cell[30]. The evaporation cell was operated in the temperature range of 1073–1123 K at a pressure of 2×10^{-10} mbar during the deposition. The quasiperiodic reconstruction of the Sn layer was unaffected by the variation of the deposition rate from 0.05 to 0.3 ML/min.

The STM measurements were carried out at a base pressure of 2×10^{-11} mbar using a variable temperature STM from Omicron GmbH and LEED using 4-grid rear view optics from OCI Vacuum Microengineering and Specs GmbH. All the STM measurements were performed at 300 K (after deposition at 300 K– 430 K) in the constant current mode using a tungsten tip that was cleaned by field emission and voltage pulse method. The tip was biased and the sample was kept at the ground potential. The STM image analysis has been performed using the SPIP software from Image Metrology. The coverages are determined in STM by measuring the fractional area of the Sn covered surface.

The photoemission measurements were performed using Phoibos analyzer from Specs GmbH with 21.2 (1253.6) eV photon energy and 3 (20) eV pass energy for ultraviolet photoemission

(X-ray photoemission) spectroscopy, respectively. The variation of the areas under Sn $3d$ and Al $2p$ core-levels has been fitted with exponential functions $I_{Sn3d}=I_{Sn3d\infty}(1-\exp(-d/\lambda))$ and $I_{Al2p}=I_{Al2p\infty}\exp(-d/\lambda)$, respectively. As in our earlier work[16, 30], we calculate the adlayer thickness from the areas under Sn $3d$ and Al $2p$ core-levels recorded under similar conditions after x-ray satellite and background subtraction using Tougaard method, and considering their respective photoemission cross-sections[31] and relativistic inelastic mean free paths[32]. The thickness is expressed in monolayers by considering its thickness to be equal to the Sn-Sn bond length (0.281 nm). The substrate temperature during deposition is 100– 300 K for photoemission and LEED studies. The coverage was also determined from STM and from the intensities of Sn MNN (430 eV) and Pd MNN (330 eV) Auger peaks.

The LEED IV curves were measured at normal incidence for four sets of bright diffraction spots (10000), (000 $\bar{1}0$), (00 $\bar{1}$ $\bar{1}0$) and (11000), as marked in Fig. 1A, averaged over the five symmetrically equivalent spots. The quantitative LEED calculations were performed using a model structure constructed using the cut-and-project method with triacontahedral acceptance domains in six dimensional hyperspace according to the Katz-Gratias-Boudard model[35]. The coordinates of Sn were relaxed in the perpendicular direction and the agreement between the experimental and theoretical LEED IV curves were tested using the Pendry reliability factor[36]. It was further modified to remove the Mn-Pd neighbors in perpendicular space, since those were found to be energetically unfavorable. The structural model consists of areas of high and low atomic density, which form a layer structure perpendicular to the five-fold axis. The distances between the atomic density minima form a Fibonacci sequence with three different distances; $s = 0.252$ nm, $m = 0.408$ nm and $l = s + m = 0.66$ nm. A quasicrystalline approximant can thus be decomposed into a sequence of slabs of three different thicknesses. Barbieri/ Van Hove symmetrized automated tensor LEED package[33] was used, where the crystal potentials for Al, Pd and Mn were characterized using phase shifts up to $l_{max}=8$ and are obtained from Barbieri/Van Hove phase shift package[34]. The other non-structural parameters included the Debye temperatures (θ_D) and the imaginary part of inner potential (V_i). The real part of V_i was assumed to be energy independent and was allowed to vary to obtain optimal agreement as it is standard procedure in LEED analysis. The energy range for the theoretical calculation was 20-220 eV.

The DFT calculations have been performed using the Vienna Ab-initio Simulation Package (VASP)[37]. VASP performs an iterative solution of the Kohn-Sham equations of density

functional theory (DFT) within a plane wave basis. We used using the semi-local PBE exchange-correlation functional[38]. The basis set contains plane waves with a kinetic energy up to $E_{\text{cut-off}} = 400$ eV. The self-consistency iterations were stopped when total energies are converged to within 10^{-6} eV. The atomic structure of the surfaces has been optimized by static relaxations using a quasi-Newton method and the Hellmann-Feynman forces acting on the atoms.

-
- [1] Penrose, R. The role of aesthetics in pure and applied mathematical research. *Bull. Inst. Math. Appl.* **10**, 266 (1974).
 - [2] Shechtman, D., Blech, I., Gratias, D. & Cahn, J. W. Metallic Phase with Long-Range Orientational Order and No Translational Symmetry. *Phys. Rev. Lett.* **53**, 1951 (1984).
 - [3] Tsai, A. P. *et al.* Alloys: A stable binary quasicrystal. *Jpn. J. Appl. Phys.* **29**, L1161 (1990); *Nature* **408**, 537 (2000).
 - [4] Talapin, D. V. *et al.* Quasicrystalline order in self-assembled binary nanoparticle superlattices. *Nature* **461**, 964 (2009).
 - [5] Förster, S. *et al.* Quasicrystalline structure formation in a classical crystalline thin-film system. *Nature* **502**, 216 (2013).
 - [6] Xiao, C. *et al.* Dodecagonal tiling in mesoporous silica. *Nature* **487**, 349 (2012)
 - [7] Ye, X. *et al.* Quasicrystalline nanocrystal superlattice with partial matching rules. *Nat. Mater.* **16**, 214 (2016)
 - [8] Park, J. Y. *et al.* High Frictional Anisotropy of Periodic and Aperiodic Directions on a Quasicrystal Surface. *Science* **309**, 1354 (2005)
 - [9] Dubois, J. M. Properties- and applications of quasicrystals and complex metallic alloys. *Chem. Soc. Rev.* **41**, 6760 (2012)
 - [10] Stadnik, Z. M. Physical Properties of Quasicrystals, Springer (1999)
 - [11] E. Kraus Y. E. Zilberberg, O. Quasiperiodicity and topology transcend dimensions. *Nature Phys.* **12**, 624 (2016)
 - [12] Sharma, H. R. *et al.* Templated three-dimensional growth of quasicrystalline lead. *Nature Commun.* **4** (2013).
 - [13] Franke, K. J. *et al.* Quasicrystalline Epitaxial Single Element Monolayers on Icosahedral Al-

- Pd-Mn and Decagonal Al-Ni-Co Quasicrystal Surfaces. *Phys. Rev. Lett.* **89**, 156104 (2002).
- [14] Ledieu, J. *et al.* Pseudomorphic Growth of a Single Element Quasiperiodic Ultrathin Film on a Quasicrystal Substrate. *Phys. Rev. Lett.* **92**, 135507 (2004).
 - [15] Shukla, A. K. *et al.* Quasiperiodic layers of free-electron metals studied using electron diffraction. *Phys. Rev. B* **79**, 134206 (2009).
 - [16] Shukla, A. K. *et al.* Growth and electronic structure of alkali-metal adlayers on icosahedral $\text{Al}_{70.5}\text{Pd}_{21}\text{Mn}_{8.5}$. *Phys. Rev. B* **73**, 054432 (2006).
 - [17] Ledieu, J. *et al.* Self-assembly, structure, and electronic properties of a quasiperiodic lead monolayer. *Phys. Rev. B* **77**, 073409 (2008).
 - [18] Smerdon, J. A. *et al.* Nucleation and growth of a quasicrystalline monolayer: Bi adsorption on the fivefold surface of $i\text{-Al}_{70}\text{Pd}_{21}\text{Mn}_9$. *Phys. Rev. B* **78**, 075407 (2008).
 - [19] Shimoda, M. *et al.* Thin Sn film induced by surface diffusion on a quasiperiodic surface of decagonal Al-Ni-Co. *Journal of Non-Crystalline Solids* **334**, 505 (2004).
 - [20] Sharma, H. R. *et al.* Real-space observation of quasicrystalline Sn monolayer formed on the fivefold surface of icosahedral Al-Cu-Fe quasicrystal. *Phys. Rev. B* **72**, 045428 (2005).
 - [21] Krajčí, M. & Hafner, J. Ab initio study of quasiperiodic monolayers on a fivefold $i\text{-AlPdMn}$ surface. *Phys. Rev. B* **71**, 184207 (2005).
 - [22] Krajčí, M. *et al.* Quasiperiodic Pb monolayer on the fivefold $i\text{-Al-Pd-Mn}$ surface: Structure and electronic properties. *Phys. Rev. B* **82**, 085417 (2010).
 - [23] Xu, Y. *et al.* *Phys. Rev. Lett.* **111**, 136804 (2013).
 - [24] Zhu, F.-f. *et al.* Epitaxial growth of two-dimensional stanene. *Nat. Mater.* **14**, 1020 (2015).
 - [25] Hafner, J. & Krajčí, M. Electronic structure and stability of quasicrystals: Quasiperiodic dispersion relations and pseudogaps. *Phys. Rev. Lett.* **68**, 2321 (1992).
 - [26] Stadnik, Z. M. *et al.* Electronic Structure of Icosahedral Alloys Studied by Ultrahigh Energy Resolution Photoemission Spectroscopy. *Phys. Rev. Lett.* **77**, 1777 (1996).
 - [27] Nayak, J. *et al.* Bulk Electronic Structure of Quasicrystals. *Phys. Rev. Lett.* **109**, 216403 (2012).
 - [28] Gierer, M. *et al.* Structural Analysis of the Fivefold Symmetric Surface of the $\text{Al}_{70}\text{Pd}_{21}\text{Mn}_9$ Quasicrystal by Low Energy Electron Diffraction. *Phys. Rev. Lett.* **78**, 467 (1997).
 - [29] Lang, N. D. and Kohn, W. Theory of metal surfaces: Charge density and surface energy. *Phys. Rev. B* **1**, 4555 (1970).

- [30] Shukla, A. K. *et al.* Versatile UHV compatible Knudsen type effusion cell. *Rev. Sci. Instrum.* **75**, 4467 (2004).
- [31] Yeh, J. J. and Lindau, I. Subshell Photoionization cross sections and asymmetry parameters: $1 \leq Z \leq 103$. *Atomic Data Nuclear Data Tables* **32**, 1 (1985).
- [32] Shinotsuka, H. *et al.* Calculations of electron inelastic mean free paths. X. Data for 41 elemental solids over the 50eV to 200keV range with the relativistic full Penn algorithm. *Surf. Interf. Anal.* **47**, 871 (2015).
- [33] Van Hove, M. A. *et al.* Automated determination of complex surface structures by LEED. *Surf. Sci. Rep.* **19**, 191 (1993).
- [34] Barbieri, A., Van Hove, M. A. <http://www.ap.cityu.edu.hk/SurfStrucInfo/SurfStrucInfo.htm>2008.
- [35] Boudard, M. *et al.* *J. Phys.: Condensed Matter* **4**, 10149 (1992).
- [36] Pendry, J. B. Reliability factors for LEED calculations. *J. Phys. C. Solid St. Phys.* **13**, 937 (1980).
- [37] Kresse, G. & Furthmuller, J. Efficiency of ab-initio total energy calculations for metals and semiconductors using a plane-wave basis set. *Comput. Mater. Sci.* **6**, 15 (1996).
- [38] Perdew, J. P., Burke, K. & Ernzerhof, M. Generalized Gradient Approximation Made Simple. *Phys. Rev. Lett.* **78**, 1396 (1997).
- [39] Maniraj, M. *et al.* Unoccupied electronic states of icosahedral Al-Pd-Mn quasicrystals: Evidence of image potential resonance and pseudogap. *Phys. Rev. B* **90**, 115407 (2014).

Acknowledgment

We thank Karsten Horn for his constructive suggestions and a careful reading of the manuscript. M.M. is grateful to the C.S.I.R., New Delhi for research fellowship. Jayita Nayak is thanked for useful discussions and help during the low temperature measurements. M.K. thanks for support from the Slovak Grant Agency VEGA (No. 2/0189/14), and from APVV (No. 15-0621). Part of the calculations were performed in the Computing Center of the Slovak Academy of Sciences using the supercomputing infrastructure acquired in under projects ITMS 26230120002 and 26210120002. LEED calculations were done at CSC IT Center for Science, Finland. This work was supported by the Academy of Finland under Grant No. 277829. Work by TAL and DLS was supported by the U.S. Department of Energy (DOE), Office of Science, Basic Energy Sciences, Materials Science

and Engineering Division. The Al-Pd-Mn substrate was synthesized at the Materials Preparation Center, at the Ames Laboratory, which is operated for the U.S. DOE by Iowa State University under contract DE-AC02-07CH11358.

Author contributions

S.R.B. planned and led the project, supervised experiments, and was engaged in analysis of the data. M.M. performed the PES and LEED; while A.R. performed the STM, LEED and Auger spectroscopy measurements. Both were involved in analysis of respective data. P.S. and V.K.S. repeated the LEED experiments to determine the IV curves and were involved in analysis of the data. K.P. performed the LEED IV calculations. M.K. performed the DFT calculations and provided explanation for the experimental observations. D.L.S. and T.A.L. grew the *i*-Al-Pd-Mn crystal. A.K.S. analyzed the XPS and LEED data. S.R.B. and M.K. wrote the paper with inputs from all other authors.

Additional information

Supplementary Information accompanies this paper.

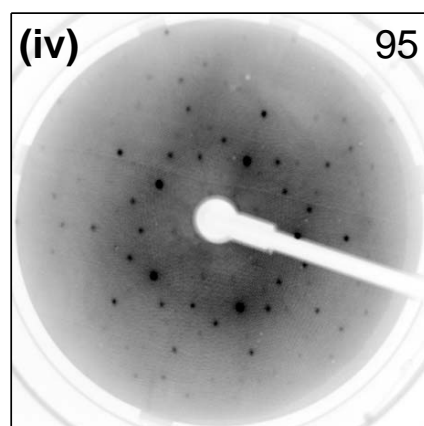
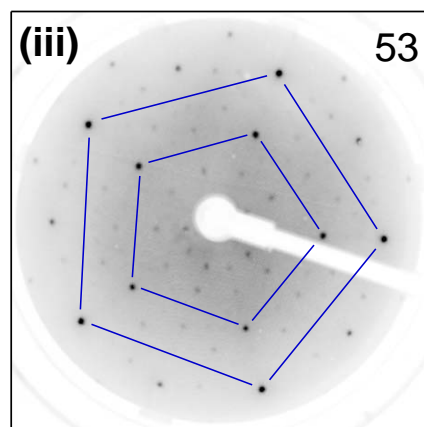
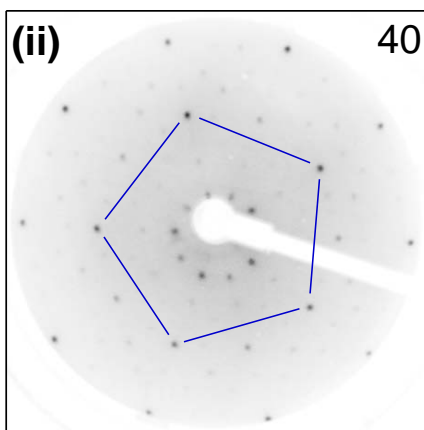
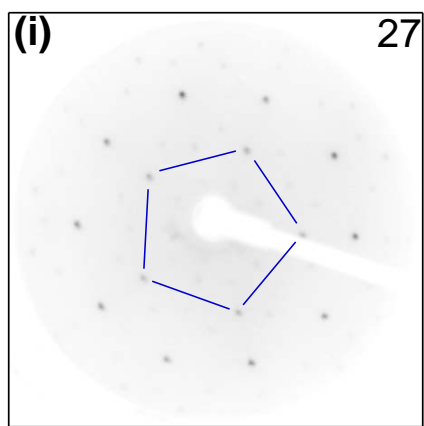
Supplementary material to the paper entitled:

Quasiperiodic Sn layer

Sudipta Roy Barman, M. Maniraj, Abhishek Rai, Marian Krajčí, Pampa Sadhukhan, Vipin Kumar Singh, Katariina Pussi, Deborah L. Schlager, Thomas A. Lograsso, Ajay Kumar Shukla

The Supplementary material contains nine figures (S1 – S9) and one video file named 5ML_Sn_Final.avi. The video file shows the sequence of LEED patterns for 1.4 nm (5 ML) Sn/Al-Pd-Mn as a function of beam energy from 60 to 120 eV, as indicated in the top left corner for each pattern.

A
0 ML



B
1.1 ML

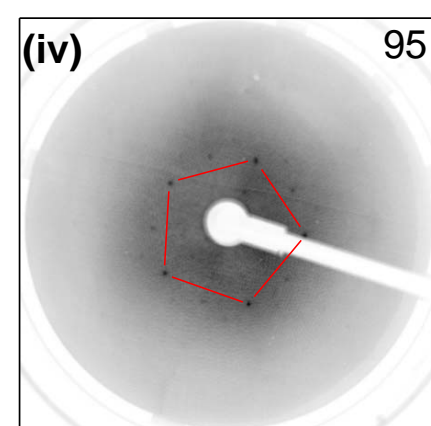
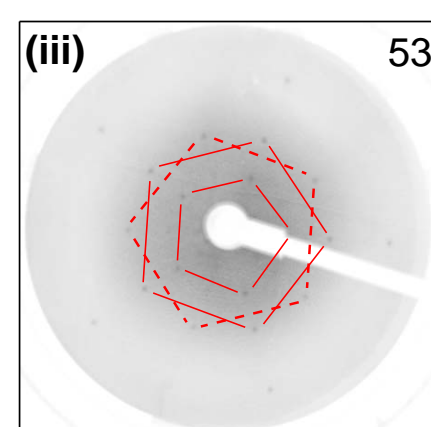
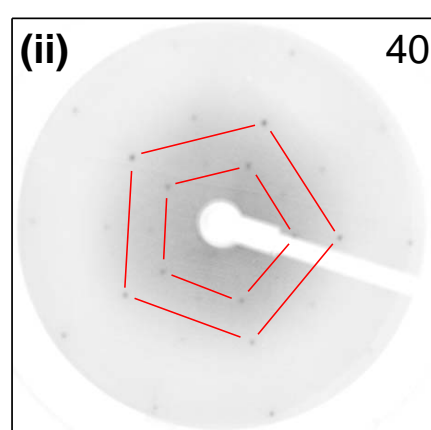
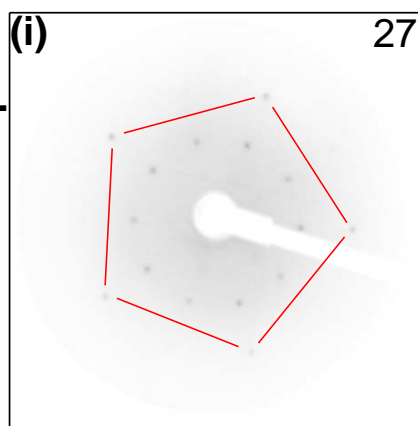


Fig. S 1. LEED patterns of **A**, *i*-Al-Pd-Mn and **B**, 1.1 ML Sn/*i*-Al-Pd-Mn for different E_p (eV), shown in the top right corner of each panel. **At $E_p = 27$ eV**, for the bare surface, the inner set of spots form a pentagon pointing downwards shown by blue lines, while the outer ring has ten spots of almost similar intensity. For 1.1 ML Sn, the opposite is observed: the inner ring has ten almost similar intensity spots, while the outer ring has five dominant spots forming a down pentagon shown by red lines (A(i) and B(i)). **At $E_p = 40$ eV**, ten spots of almost similar intensities are observed for the bare surface in the innermost ring, while 1.1 ML Sn adlayer shows a down pentagon (red lines) that is larger in size. In the outer set, an up pentagon (blue lines) is prominently observed in *i*-Al-Pd-Mn; whereas a down pentagon (red lines) is observed in the Sn adlayer (A(ii) and B(ii)). **At $E_p = 53$ eV**, *i*-Al-Pd-Mn exhibits two dominant down pentagons (blue lines) (A(iii)), with two sets of 10 spots as inner rings. On the other hand, the Sn adlayer exhibits an inner down pentagon and two outer pentagons (red solid and dashed lines) (b(iii)). **At $E_p = 95$ eV** (A(iv) and B(iv)), only one prominent down pentagon (red lines) is observed.

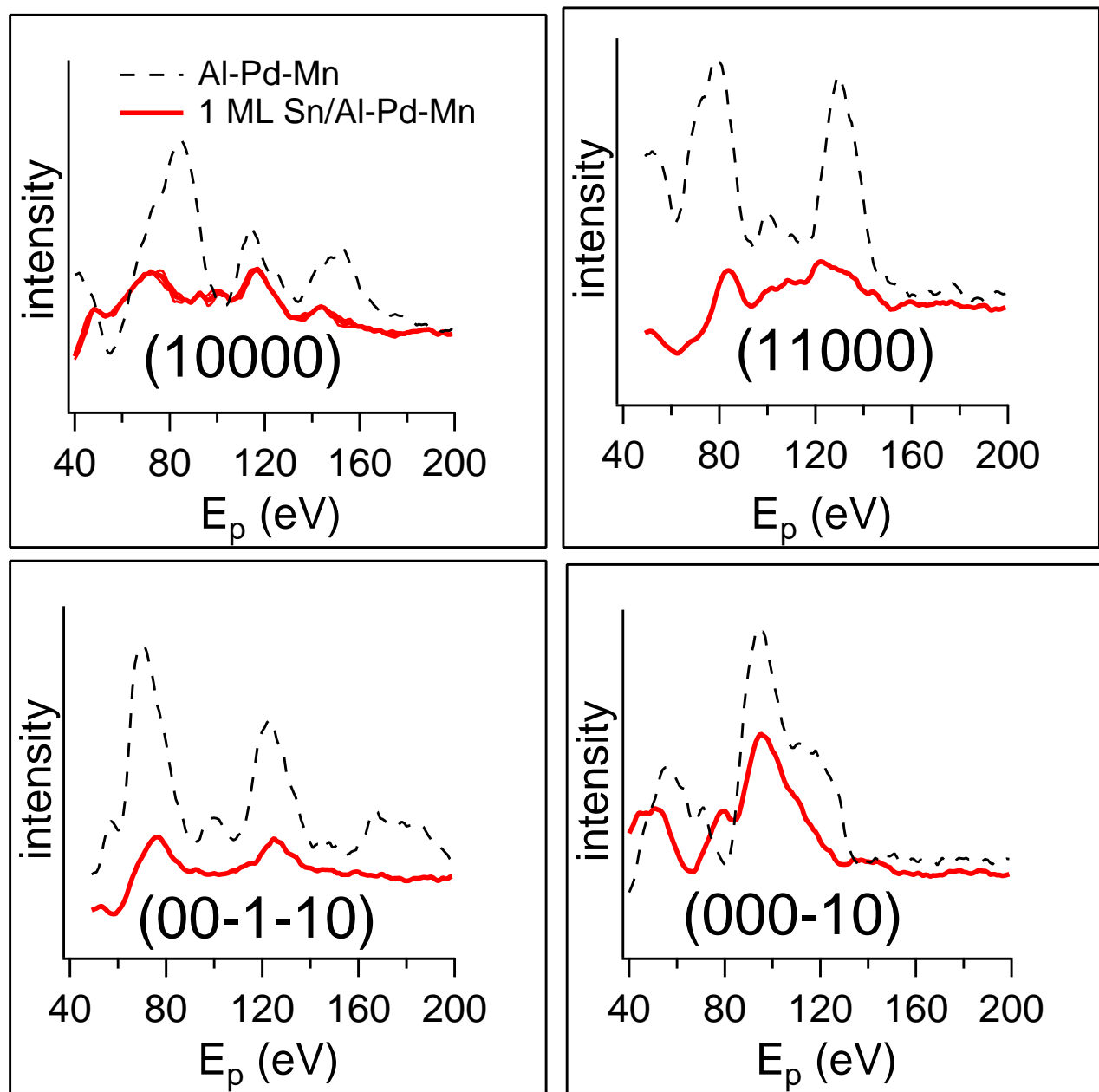


Fig. S 2: Experimental IV curves for 1 ML Sn/ i -Al-Pd-Mn compared with those of substrate i -Al-Pd-Mn for (10000), (11000), (00 $\bar{1}\bar{1}$ 0) and (000 $\bar{1}$ 0) LEED spots.

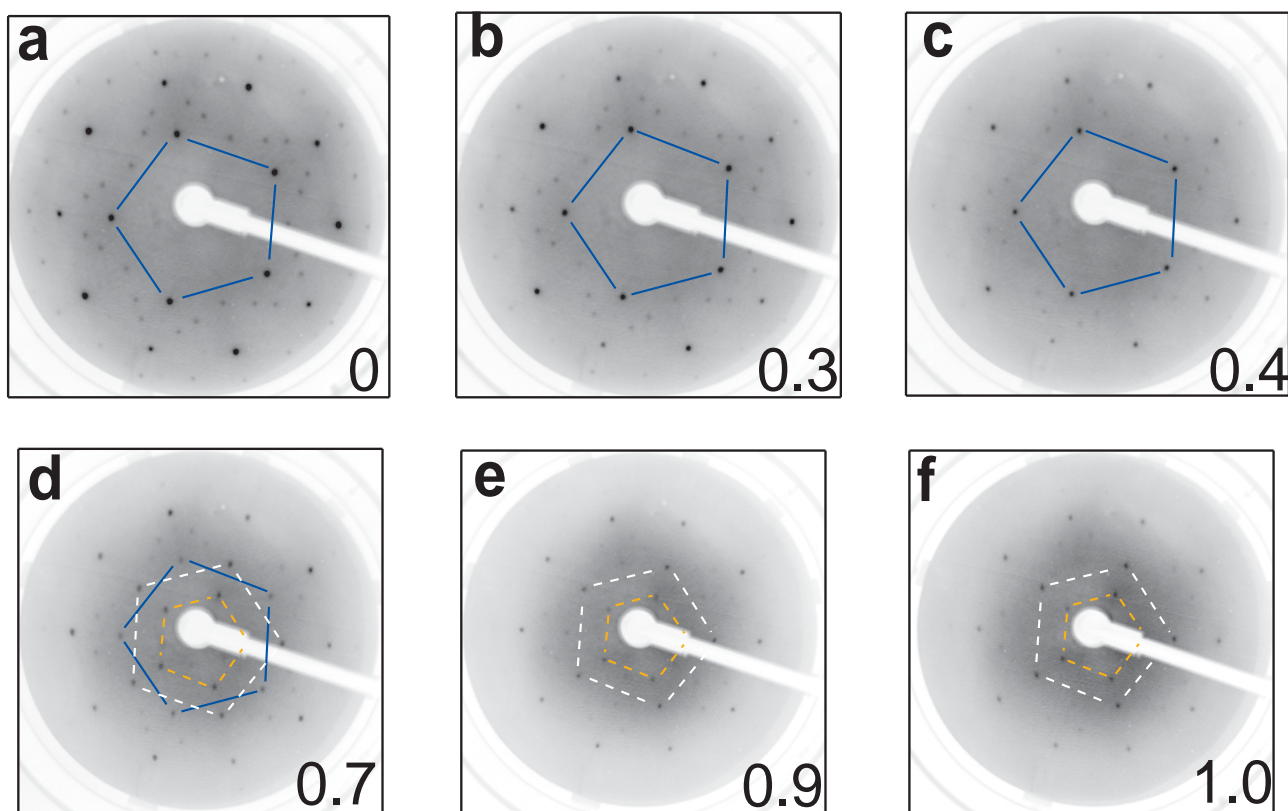


Fig. S 3: Low energy electron diffraction patterns of Sn/*i*-Al-Pd-Mn as a function of Sn coverage at room temperature (RT).

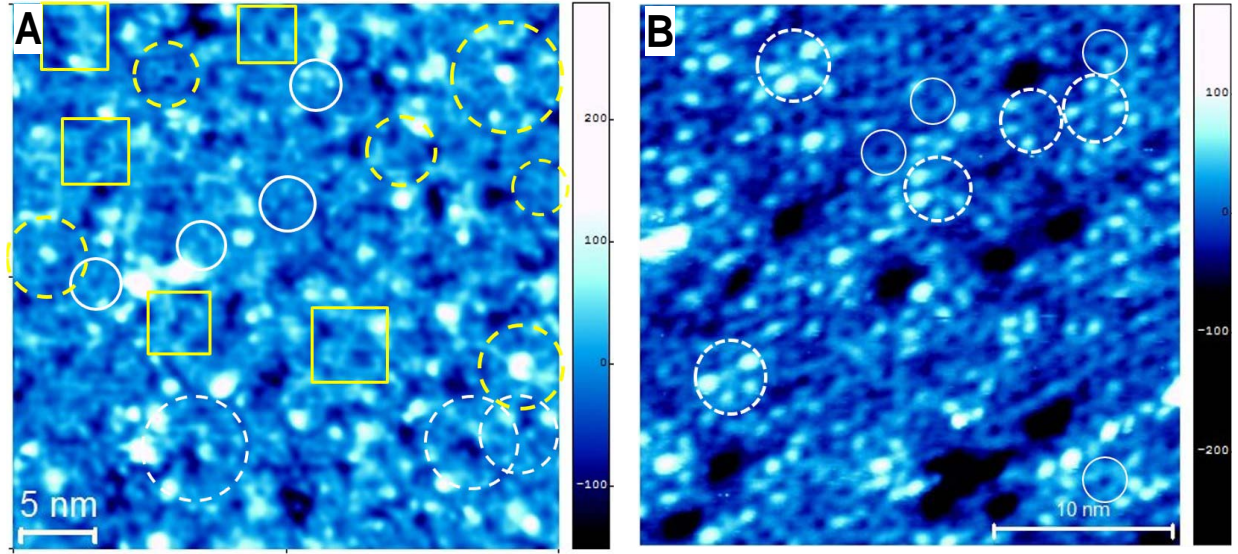


Fig. S 4: **(A)** Constant current high resolution STM image with $I_T = 0.2$ nA tunneling current and $U_T = 1.5$ V bias voltage at RT for 1 monolayer (ML) Sn/*i*-Al-Pd-Mn after low-pass Fourier transform filtering compared with that of **(B)** *i*-Al-Pd-Mn ($I_T = 0.1$ nA, $U_T = 1.5$ V). The white dashed and white continuous line circles enclose white flowers (WF) and dark stars (DS), respectively in the latter.

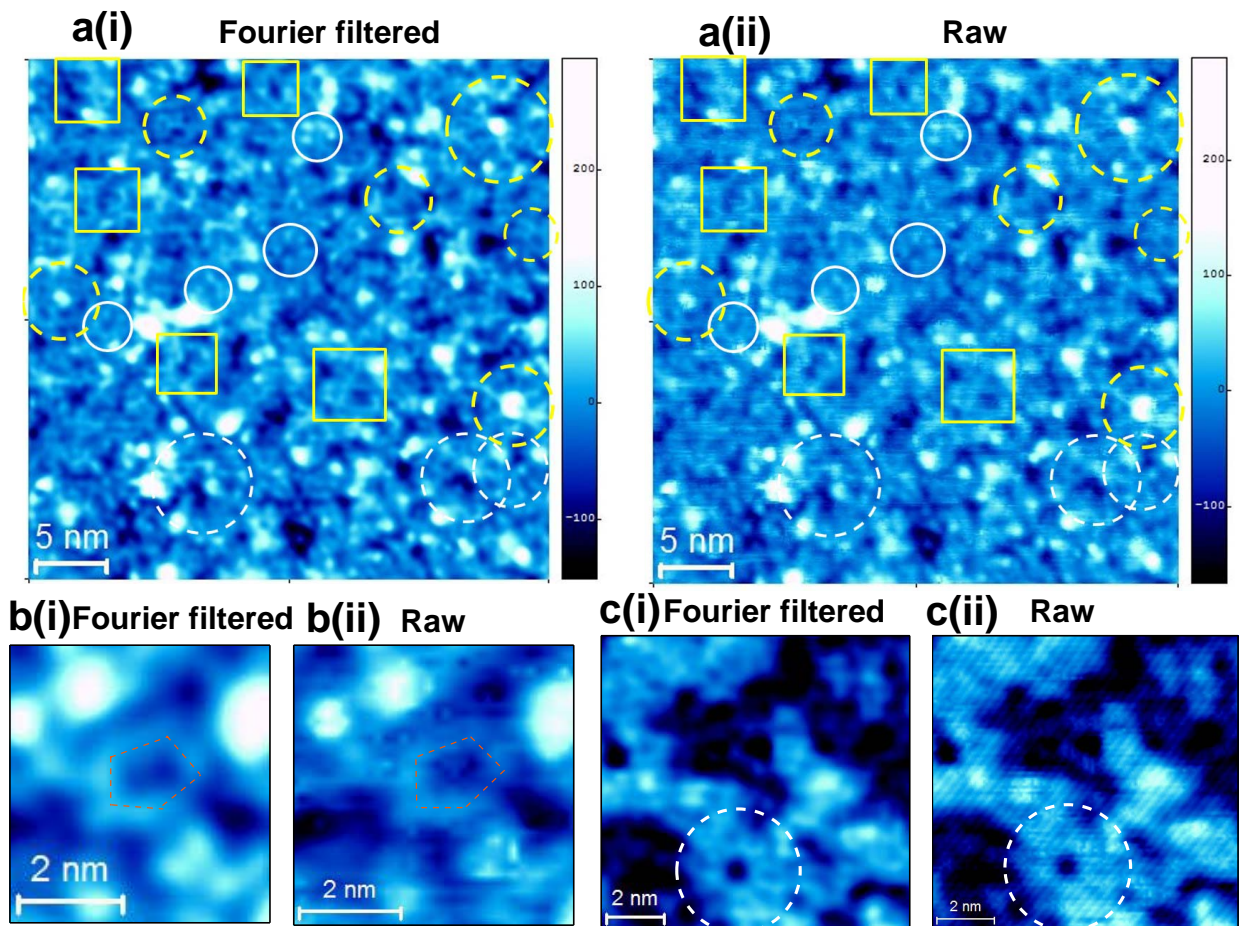


Fig. S 5: A comparison to show the feature-wise correspondence between the Fourier filtered [a(i), b(i) and c(i)] and the corresponding raw [a(ii), b(ii) and c(ii)] STM images of 1 and 0.6 ML Sn/*i*-Al-Pd-Mn to confirm that no artifact induced by Fourier filtering. The color scale with the height in picometers is shown on the right. These Fourier filtered STM images are shown also in Fig. 2(a), (d) and (i), respectively in the paper. The Fourier filtering using a low pass filter removes the high frequency noise in the raw image and thus improves its quality.

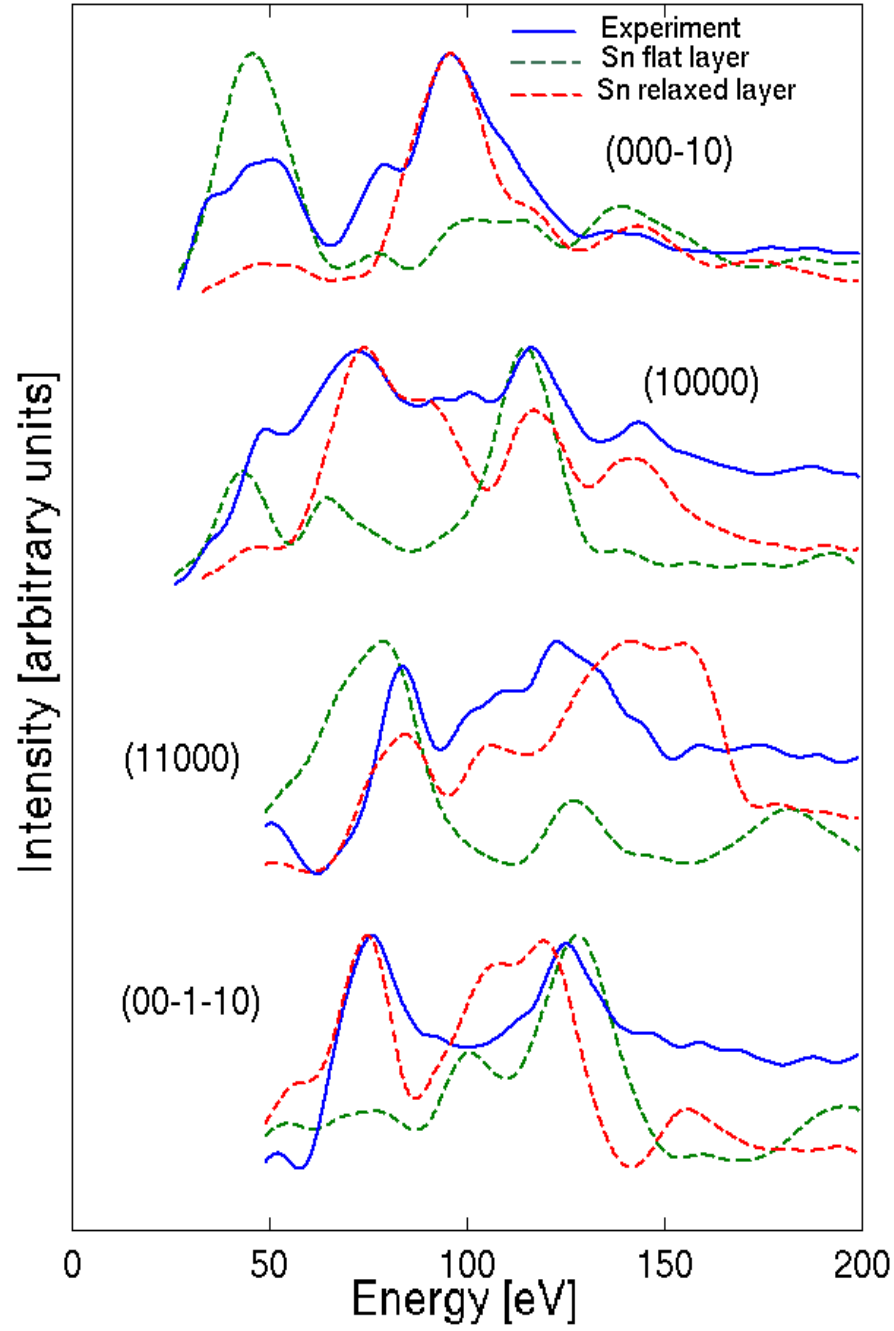


Fig. S 6: Comparison of experimental (blue continuous line) IV curves for 1 ML Sn/*i*-Al-Pd-Mn with the theoretical calculation with Sn flat layer (green dashed line) shows that unless the Sn adlayer is relaxed, the IV cannot be explained. Also shown is the theoretical IV for the Sn relaxed layer that results in its buckling (red dashed line, also shown in Fig. 1I of the manuscript). The indexes of spots for which IV is performed are indicated and some of the curves have been shifted along the vertical axis for clarity of presentation.

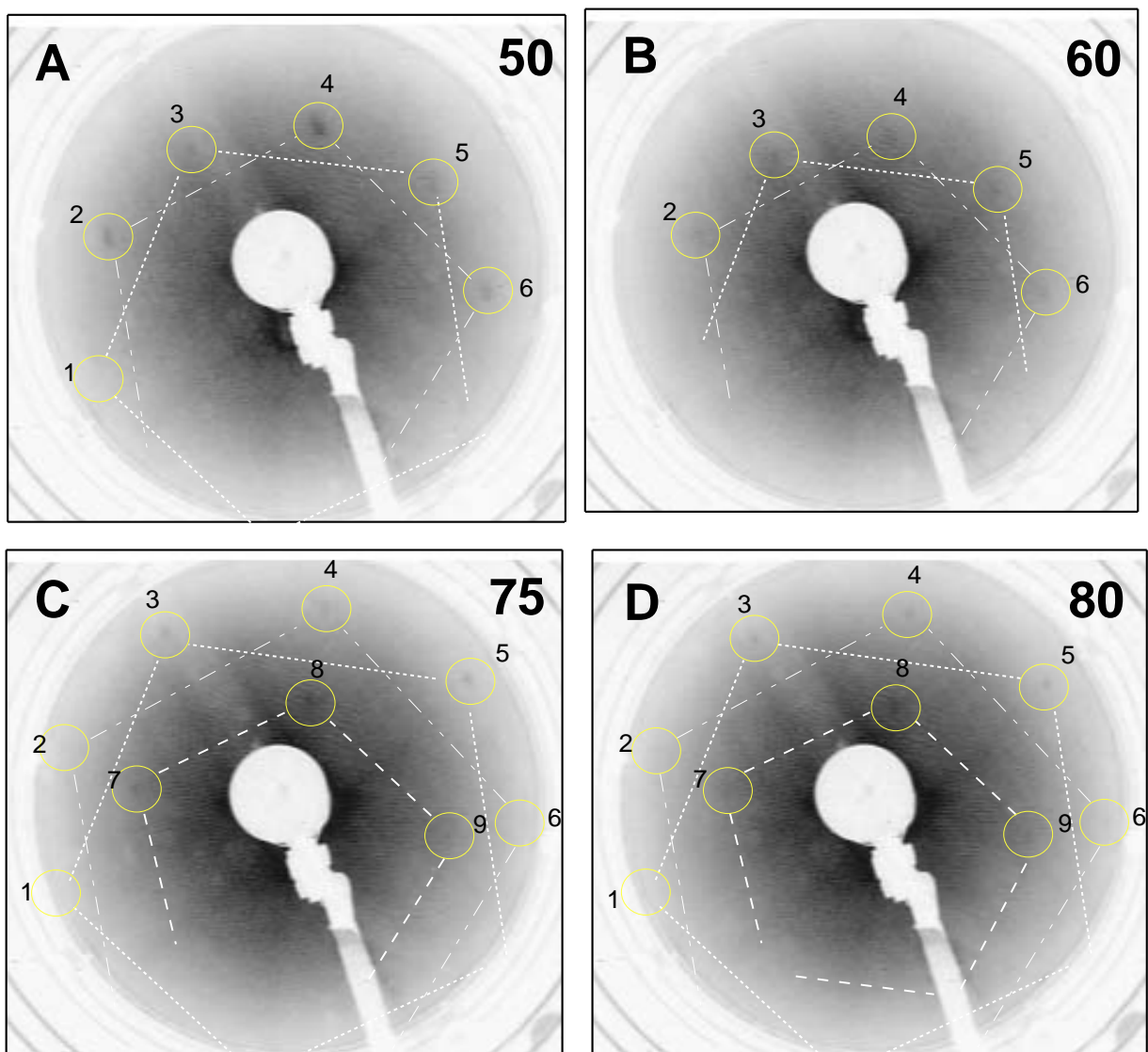


Fig. S 7: **A-D**, LEED patterns at different beam energies (indicated at top right corner in eV) for 5 ML Sn/*i*-Al-Pd-Mn.

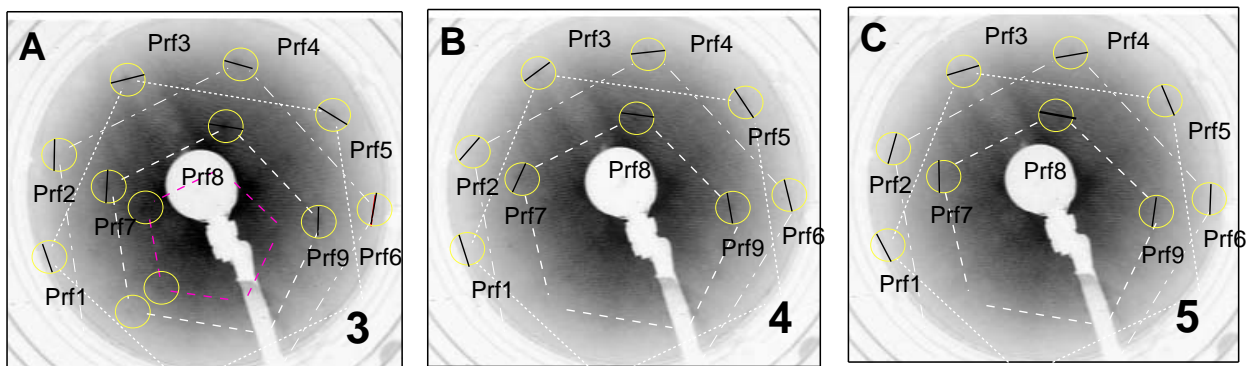


Fig. S 8: **A-C**, LEED patterns at different Sn coverage (indicated at bottom right corner in ML) showing the lines named Prf1 through Prf9 along which the intensity profiles are calculated for spots 1 through 9.

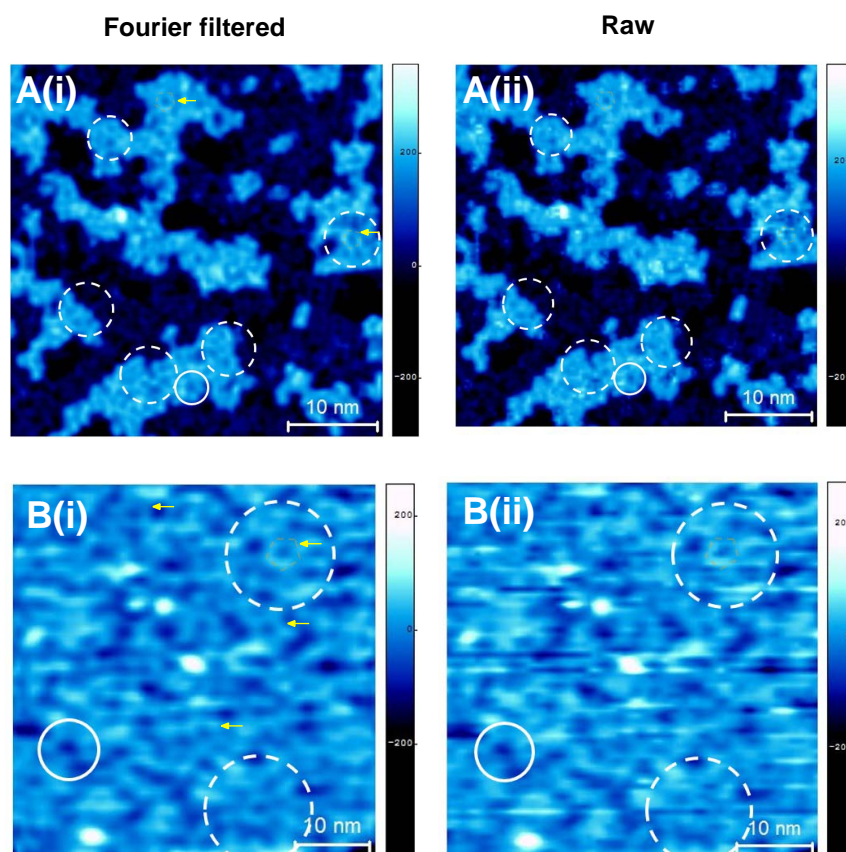


Fig. S 9: A comparison to show the feature-wise correspondence between the Fourier filtered [A(i) and B(i)] and the corresponding raw [A(ii) and B(ii)] STM images of 1.4 and ≈ 2 ML Sn/*i*-Al-Pd-Mn to confirm that no artifact induced by Fourier filtering.